Impact of rock microstructures on failure processes
- Numerical study based on DIP technique

Qinglei Yu [1,2a], Wancheng Zhu [*1,2], Chun'an Tang [3b] and Tianhong Yang [1,2c]

[1] *Key Laboratory of Ministry of Education on Safe Mining of Deep Metal Mines, Northeastern University, Shenyang, 110819, China*
[2] *Center for Rock Instability and Seismicity Research, Northeastern University, Shenyang, 110819, China*
[3] *Center for Rock Instability and Seismicity Research, Dalian University of Technology, Dalian 116024, China*

Abstract. It is generally accepted that material heterogeneity has a great influence on the deformation, strength, damage and failure modes of rock. This paper presents numerical simulation on rock failure process based on the characterization of rock heterogeneity by using a digital image processing (DIP) technique. The actual heterogeneity of rock at mesoscopic scale (characterized as minerals) is retrieved by using a vectorization transformation method based on the digital image of rock surface, and it is imported into a well-established numerical code Rock Failure Process Analysis (RFPA), in order to examine the effect of rock heterogeneity on the rock failure process. In this regard, the numerical model of rock could be built based on the actual characterization of the heterogeneity of rock at the meso-scale. Then, the images of granite are taken as an example to illustrate the implementation of DIP technique in simulating the rock failure process. Three numerical examples are presented to demonstrate the impact of actual rock heterogeneity due to spatial distribution of constituent mineral grains (e.g., feldspar, quartz and mica) on the macro-scale mechanical response, and the associated rock failure mechanism at the meso-scale level is clarified. The numerical results indicate that the shape and distribution of constituent mineral grains have a pronounced impact on stress distribution and concentration, which may further control the failure process of granite. The proposed method provides an efficient tool for studying the mechanical behaviors of heterogeneous rock and rock-like materials whose failure processes are strongly influenced by material heterogeneity.

Keywords: rock heterogeneity; digital image processing (DIP) technique; rock failure mechanism; numerical simulation

1. Introduction

Rock is a heterogeneous geomaterial that has a composite microstructure in form of mineral grains, voids, microcracks and weak interfaces. These individual components of rock usually have different mechanical and physical properties and different responses when subjected to internal or

∗Corresponding author, Professor, E-mail: zhuwancheng@mail.neu.edu.cn
[a] Associate Professor, E-mail: yuqinglei@mail.neu.edu.cn
[b] Professor, E-mail: tca@mail.neu.edu.cn
[c] Professor, E-mail: yangtianhong@mail.neu.edu.cn

external loadings, thus the behaviors of rock are strongly influenced by this heterogeneous microstructure. How to describe rock heterogeneity and furthermore considering its impact on the rock fracture behavior is a key issue to be seriously concerned. To this end, it is to develop a digital image processing-based (DIP-based) technique to take the actual heterogeneity of rock into account in the simulation of rock failure process that defines the objective of this work.

During the past decades, with the rapid development of computing power, interactive computer graphics and topological data structures, mesoscopic numerical models coupled with the heterogeneous material properties have become an effective approach to tackling the complicated fracture behavior of rock-like heterogeneous materials (Yuan and Harrison 2006). For example, the non-linear rule-based model (Blair and Cook 1998), the lattice model (Van Mier 1997, Chinaia *et al*. 1997, Schlangen and Garboczi 1997), the granular model (Malan and Napier 1995, Fairhurst 1997), the bonded particle model (Potyondy and Cundall 2004, Potyondy *et al*. 1996) and the local degradation model (Fang and Harrison 2002) have been established to simulate the fracture process of quasi-brittle materials such as rock and concrete. Most importantly, rock failure process analysis (RFPA) model developed by Tang and his co-researchers (Tang 1997, Zhu and Tang 2002, 2004, Tang *et al*. 2000) has also been a prevailing numerical tool for studying the progressive failure process of rock and other quasi-brittle materials. Recently, these models are improved and some new model are also proposed, such as the cellular automaton method improved by Pan *et al*. (2012) and Yan *et al*. (2014), the damage-based numerical model proposed by Molladavoodi and Mortazavi (2011) and Mortazavi and Molladavoodi (2012), the multi-scale rate dependent crack model developed by Karamnejad *et al*. (2013), the mesh-free smoothed particle hydrodynamics (SPH)-based model developed by Ma *et al*. (2011), the improved lattice model by Zhao *et al*. (2012), as well as the discontinuum-based model improved by Kazerani *et al*. (2013). Moreover, it is notice that the RFPA model is also developed into a three dimensional one (Liang *et al*. 2012).

In these mesoscopic numerical models (Blair and Cook 1998, Van Mier 1997, Chinaia *et al*. 1997, Schlangen and Garboczi 1997, Malan D and Napier J 1995, Fairhurst 1997, Potyondy and Cundall 2004, Potyondy *et al*. 1996, Fang and Harrison 2002, Tang 1997, Zhu and Tang 2002, Zhu and Tang 2004, Tang *et al*. 2000), including improved or newly developed models (Pan *et al*. 2012, Yan *et al*. 2014, Molladavoodi and Mortazavi 2011, Mortazavi and Molladavoodi 2012, Karamnejad *et al*. 2013, Ma *et al*. 2011, Zhao *et al*.2012, Kazerani 2013, Liang *et al*.2012), the rock microstructures have to be taken into account as the basic prerequisite, in order to capture the rock failure mechanism associated with rock heterogeneity. In these models, rock specimen is usually discretized into elements at the mesoscopic level, such as grid cell, truss element or beam element, circular hard particle with or without bonded strength. In addition, the material properties of these heterogeneous components in the numerical specimen are assumed to conform to a statistical distribution and are assigned by Monte-Carlo method or randomly. The behavior of the basic elements is governed by the basic laws or rules (Blair and Cook 1998). For example, in previous version of RFPA, heterogeneity of numerical model is implemented by assigning statistical distribution of properties according to the Weibull distribution (Weibull 1951) and elastic damage mechanics is used to describe the constitutive law of mesoscopic elements (Zhu and Tang 2004). As stated by Blair and Cook (1998) before, the statistical methods have emerged as a promising technique for the analysis of heterogeneous rock materials. Statistics-based micromechanical models have been prevailing in rock mechanics mainly because it was too difficult to look inside the rock materials and acquire accurate measurements of actual geometrical distributions of minerals and other components in rock solids (Yue *et al*. 2003). However, in all of these models, microstructures of rock are virtually generated by using statistical or random

distribution, which may misinterpret critical local-scale heterogeneities in the rock because it is usually difficult to adequately specify the statistical distribution parameters in order to reproduce actual microstructures in rock (Zhu *et al*. 2006). It is believed that the virtual heterogeneity and microstructure generated from the statistical equivalence cannot exactly represent the actual heterogeneity and microstructures of rock.

In order to have a better representation of heterogeneity of rock and rocklike materials, many researchers attempt to apply digital image processing (DIP) techniques to characterizing and measuring the heterogeneity and microstructures of rock and rock-like materials. Digital image retrieved from fresh cross-section of rock sample or rock-like materials by camera or other digital imaging equipment can truly reflect the geometrical distributions of different materials through different degrees of gray levels or colors. The DIP technique has also been successfully used in rock mechanics. For instance, Reid and Harrison (2000) used a series of DIP techniques to develop a methodology for the semi-automated detection of discontinuity traces in grayscale digital images of rock mass exposures. Kemeny *et al*. (2003) presented the use of digital imaging combined with laser scanning technologies for rocks fracture characterization. Lemy and Hadjigeorgiou (2003) developed a digital face mapping system used to construct discontinuity trace maps from photographs of rock faces, in which general-purpose DIP techniques (e.g., grey-scale threshold, grey-scale smoothing and edge detection) are used for fast and safe acquisition of discontinuity network data. Yue and Morin (1996) used DIP techniques for aggregate orientation in asphalt concrete mixtures. In those studies, DIP techniques are mainly used for quantitative analysis of rock heterogeneities and observations of geometrical features on rock surfaces.

Recently, DIP techniques have been incorporated into numerical method and mechanical modeling. Yue *et al*. (2003 and 2004) developed a DIP-based finite element method for the two-dimensional mechanical analysis of geomaterials by actually taking into account their material heterogeneities and microstructures. It is also applied to analyze the effect of minerals on the mechanical response of granites under loading (Yue *et al*. 2003). Chen *et al*. (2004) applied DIP techniques to acquiring the internal structures of different mineral distribution from color rock image and incorporated them into the finite difference software package FLAC for mechanical analyses and failure prediction. Although Chen *et al*. (2004) used the developed method to predict the failure of granite in indirect tensile tests, their studies mainly focused on the effect of actual heterogeneity on mechanical behaviors of rock at pre-peak stage, little care is taken on the failure process and damage evolution after the peak strength of rock. In this study, we integrate DIP technique characterized heterogeneity into a well-established code RFPA (Zhu and Tang 2004, Tang *et al*. 2000) and focus on studying the effect of actual heterogeneity on the complete damage evolution and failure process, thus clarifying the rock failure mechanism governed by the rock heterogeneity at the grain scale.

In this paper, firstly, the general-purpose DIP technique is employed to acquire the actual heterogeneity and microstructures from the color image of the cross-section of rock sample. Secondly, the digitized image data that contain rock heterogeneity information is directly imported into RFPA by a vecterized algorithm. Finally, three conventional rock mechanics tests of rock specimens are numerically simulated in order to clarify the effect of rock heterogeneity on the complete deformation, damage and failure mechanism.

2. Characterization of the microstructure of rock

2.1 Digital image processing (*DIP*) technique

DIP is the term applied to convert an image into a digital form that can be stored in computer, and then apply mathematical algorithms to extract significant information from the image. Digital image of rock can be obtained by digitized equipment, such as digital camera, scanner, X Ray CT machine. In computer, the digital image is composed of a rectangular array of pixels. Each pixel is the intersection of area of a horizontal scanning line with a vertical scanning line. For a gray image, each pixel is assigned an integer value ranging from 0 to 255, which is used to present the brightness at this point, and named as gray level. For true color images, each pixel has three integer variables in term of the format of RGB (where R, G, B stand for red, green, blue, respectively) and three integer values ranging from 0 to 255 respectively, are used to represent the red, green and blue levels at each pixel. The digital image is composed of an array of pixels with different gray levels or RGB values, and different gray levels or RGB values represent different internal microstructures information of the image. Therefore, the digital image can be expressed as a discrete function $f(i, j)$ in the i and j Cartesian coordinate system, which is used as the base of the DIP

$$f(i,j) = \begin{bmatrix} f(1,1) & f(1,2) & \cdots & f(1,M) \\ f(2,1) & f(2,2) & \cdots & f(2,M) \\ \vdots & \vdots & & \vdots \\ f(N,1) & f(N,2) & \cdots & f(N,M) \end{bmatrix} \tag{1}$$

where i varies from 1 to N, and j from 1 to M, and M and N are the number of pixels in the horizontal and vertical directions, respectively. For RGB color images, the image data consist of three discrete functions $f_n(i, j)$, where $n = 1, 2$ or 3.

Color images of rock, from digital camera or other image obtaining equipment, maybe contain more abundantly structural information of rock compared with gray images. Therefore, DIP technique for color images is to acquire fine heterogeneity information from the color image of rock and the discrete function $f_k(i, j)$ of the digital images.

DIP techniques usually include noise removal, contrast enhancement, segmentation, edge detection and feature extraction of images. In this paper, multi-threshold segmentation method is adopted to identify and characterize the rock heterogeneity. Moreover, noise removal and contrast enhancement are also necessary as the pre-treatment of digital image in order to improve the quality of image segmentation. Image segmentation refers to the process of assigning a label to every pixel in an image such that pixels with the same label share certain visual characteristics. The goal of segmentation is to simplify and/or change the representation of an image into something that is more meaningful and easier to analyze. For a rock image, image segmentation is to identify the internal components of rock and class them into groups with their own labels, such as mineral grains with different colors and different shapes, pores and micro-cracks. Multi-threshold segmentation can be expressed using the following equation

$$g(x,y) = k, \quad \text{if} \quad T_{k-1} \leq f(x,y) < T_k, \quad k = 1, 2, \cdots, n \tag{2}$$

where $g(x, y)$ is the value of pixels of the output segmented image, $f(x, y)$ is the value of pixels of the original image, T_k is the image segmentation threshold, and k is the label. Here we assume that the number of thresholds is n.

By using Eq. (2), image segmentation is completed and every kind of minerals and components in the rock image are assigned a label to be identified. Accordingly, the characterization of rock

heterogeneity will be implemented accurately.

2.2 Image analysis and rock heterogeneity characterization

Fig. 1(a) shows the digital image of a granite sample obtained by a digital camera, based on which the different components of minerals can be distinguished. According to mineral analysis, it deems that there are three main minerals in granite, namely quartz, feldspar and mica. The size of the granite sample is 50 mm × 100 mm, and the resolution of the image is 150 × 300 pixels. That is to say, the side length of a pixel is longer than 0.33 mm. In order to capture the heterogeneous details of rock surface as accurate as possible, the higher resolution of the digital image is taken. The microstructure of the granite sample is finely represented by the RGB value of each pixel. As shown in Fig. 1(b), a small rectangle area of this image on the top right is isolated and enlarged to illustrate the local i and j coordinate system and the image data structure.

Multi-threshold segmentation is used to identify the three mineral grains. The key to image segmentation is the specification of thresholds, where the two thresholds must be determined in order to identify three mineral grains. In this respect, a computer program is compiled based on Visual C++ platform for image analysis and image segmentation. In this program, the Hue, Saturation and Intensity (HSI) color space, as an alternative to the RGB color space, is selected for image segmentation because it is close to how humans perceive colors (Gonzalez and Woods 1992). The hue component (H) represents repression related to the dominant wavelength of the color stimulus. Therefore, the hue is the domain color perceived by human beings. The saturation
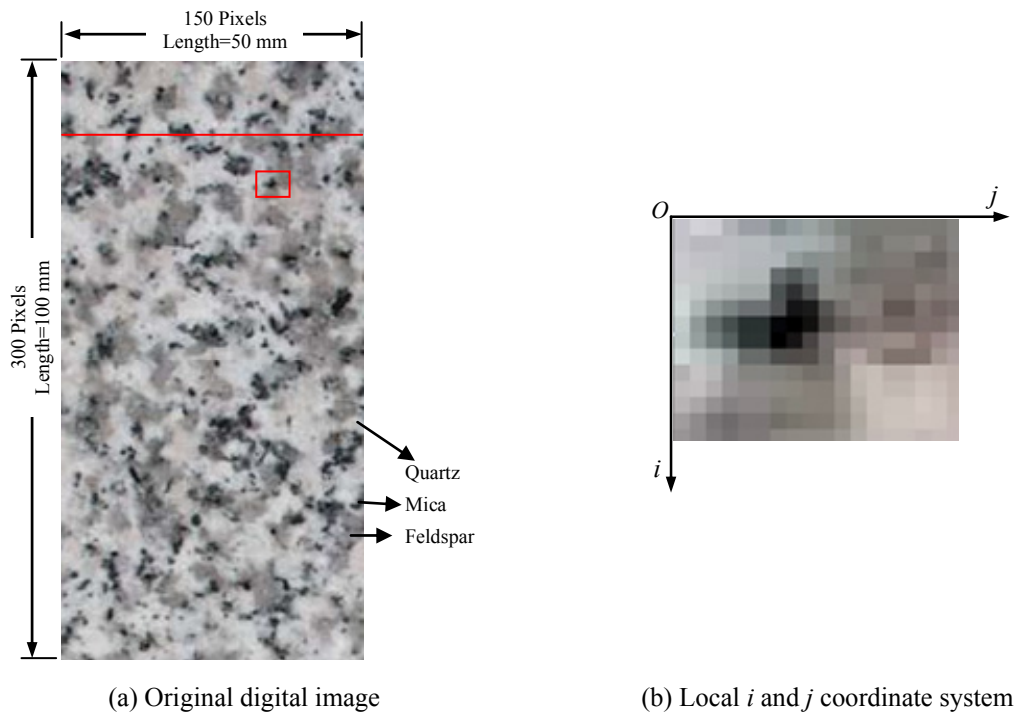

(a) Original digital image   (b) Local i and j coordinate system

Fig. 1 The digital image of an ordinary granite

component (*S*) represents how strongly the color is polluted with white. The intensity component (*I*) stands for brightness or lightness and is irrelevant to colors. In general, hue, saturation, and intensity are obtained by transformation formulae by converting numerical values of *R*, *G*, and *B* in the RGB color space to the HSI color space. The value of *S* varies from 0 to 1, the value of *I* varies from 0 to 255, and the value of *H* varies from 0 to 360. The values of the three color components are normalized to be from 0 to 255.

Figs. 2(a)-(c) show the variation of the discrete function $f_k(i, j)$ of the three components *H*, *S* and *I* along the specified red line at a 12 mm distance from the top end (as shown in Fig. 1(a)),

(a) *H* values

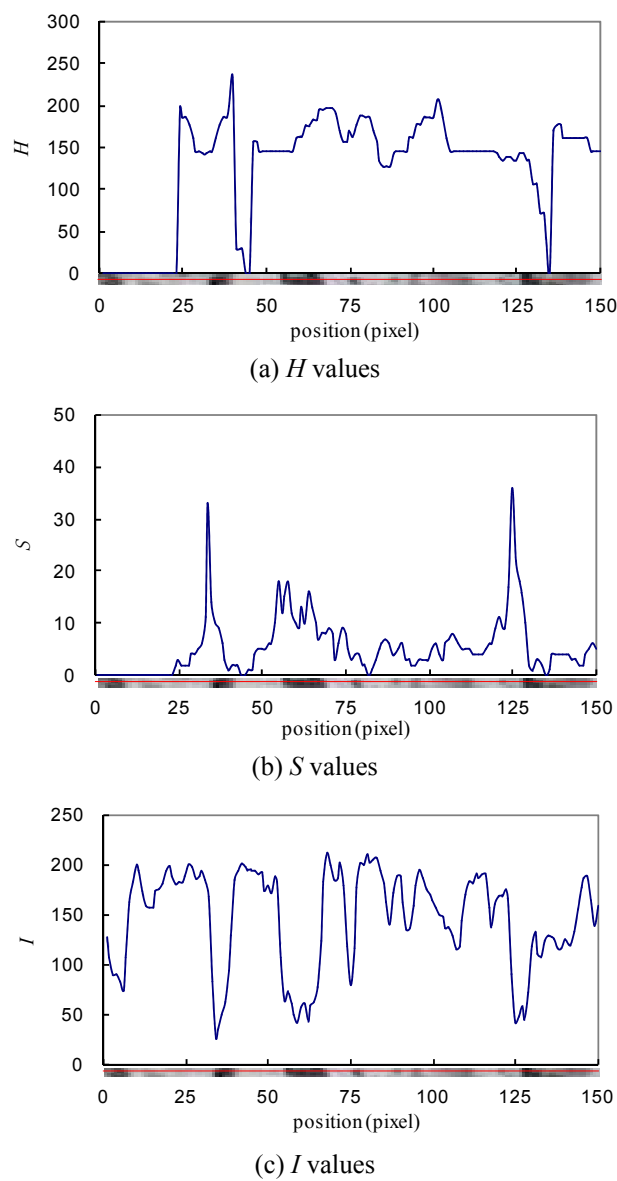(b) *S* values

(c) *I* values

Fig. 2 Color components in HSI color space on the red line as specified in Fig. 1(a)
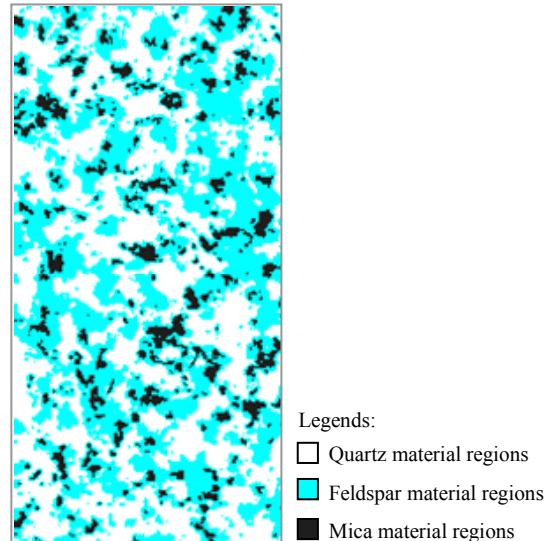
Fig. 3 Digital image characterization of the heterogeneity of granite

respectively. It can be seen that the curve of each discrete function has different characteristics, based on which the distribution of mineral grains could be distinguished. By comparing the characteristics of each curve (Figs. 2(a)-(c)) with the distribution of mineral grains, it is found that I values in Fig. 2(c) agree well with the spatial location of mineral grains. In Fig. 1(a), along the red line, there exist four concentrated parts of mica. In the *j*-coordinate, their ranges are from 3 to 7, from 33 to 39, from 55 to 66 and from 124 to 130, respectively. For the mica is dark gray and I value is lower than another two mineral grains (Fig. 2(c)). By analyzing the characteristics of the curve as shown in Fig. 2(c), it is found that I values of most mica grains are below 100, thus first threshold for image segment T_1 is selected as 100. However, I values of quartz and feldspar are rather close and the threshold between them are not easily distinguished. In this respect, we compared the characteristic of the curve (Fig. 2(c)) with the location of the two mineral grains on the red line carefully, and also combined with the trial-and-error estimation, the second threshold T_2 is estimated as 170.

According to Eq. (2) with these two thresholds, three minerals are determined and shown in Fig. 3 using image segmentation technique, where the quartz, mica and feldspar are shown as white, black and cyan, respectively. In the numerical simulation of RFPA code, each kind of mineral grains is assigned with different material parameters in order to examine the effect of the mineral composition on the mechanical behavior and failure process of rock.

2.3 Geometry vectorization of the microstructure of rock

A digital image consists of a rectangular array of pixels, and each pixel occupies a square area as shown in Fig. 1(b). So each pixel can be considered as a quadrangle element of finite element method (FEM). For each square element, its four corner coordinates can be calculated by the corresponding positions in a digital image plus the scale distance d (Fig. 4(a)). Fig. 4 shows an illustration of transformation from the image structure to coordinates of finite elements, which are given by

(a) Pixels in the digital image(as shown in Fig. 2)   (b) FEM mesh
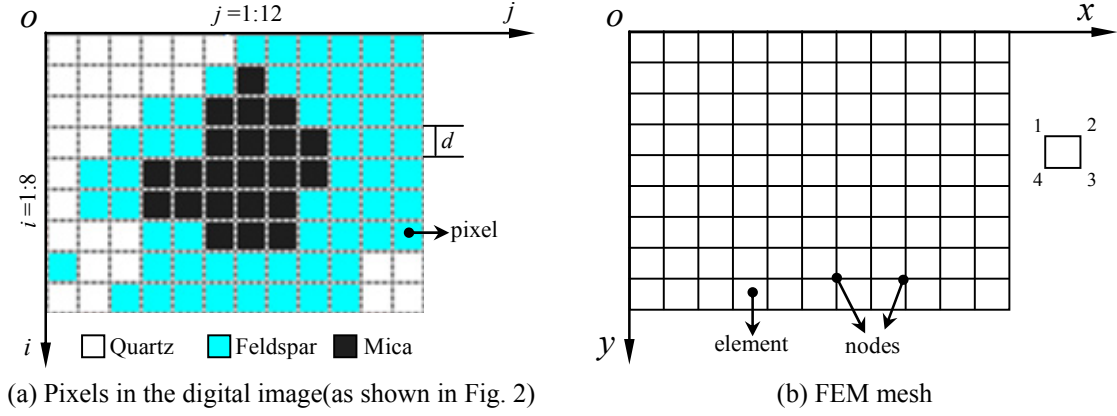
Fig. 4 An illustration of transformation from pixel to mesh

$$
\left.
\begin{aligned}
x_1 &= (j-1) \times d, & y_1 &= (i-1) \times d \\
x_2 &= j \times d, & y_2 &= i \times d \\
x_3 &= j \times d, & y_3 &= (i+1) \times d \\
x_4 &= (j-1) \times d, & y_4 &= (i+1) \times d
\end{aligned}
\right\}
\tag{3}
$$

where i and j are the coordinates of a pixel in the digital image; x_n and y_n are the coordinates of the nth node of the corresponding square grid, where $n = 1, 2, 3$ and 4, and the node sequence is shown in Fig. 4(b); d is the width of the scanning line, and it can be defined by

$$
d = \frac{w_r}{w} = \frac{h_r}{h}
\tag{4}
$$

where w and h are the width and height of the image, respectively; w_r and h_r are the width and height of the 2D granite sample.

By using Eqs. (3) and (4), we can transform the image structure data into a square mesh data easily. A program embedded in the RFPA code is developed for implementing this work automatically so that the image microstructure can be directly imported into the RFPA code.

This kind of transformation method to get the finite element mesh based on the digital image is simple and easy. However, its main disadvantage may be related to the number of the finite elements. If the number of a digital image is 1000×1000 pixels, and the total number of square element meshes will be equal to 1,000,000. Finite element analysis with such large number of finite elements would require such long computational time and storage space that PC cannot afford this kind of numerical analysis.

2.4 Brief introduction to RFPA code

RFPA^{2D} is a two-dimensional code that can simulate the fracture and failure process of quasi-brittle materials such as rock (Zhu and Tang 2004). To model the failure of rock-like material, the rock medium is assumed to be composed of many mesoscopic elements whose material properties are different from one to another. The finite element method is employed to

obtain the stress fields in the mesoscopic elements. Elastic damage model is used to describe the constitutive law of the mesoscopic elements, and the maximum tensile stress criterion and the Mohr-Coulomb criterion are utilized as damage thresholds for tensile damage and shear damage, respectively. In the previous version of the RFPA code, the mechanical properties of mesoscopic elements are assumed to conform to a given Weibull distribution (Weibull 1951) and assignment of material properties is according to this statistical function. In this paper, as an alternative, DIP technique is employed to build a numerical model that can take into account the actual microstructure of rock, including the properties of mineral constituents.

Initially an element is considered elastic, with elastic properties defined by Young's modulus and Poisson's ratio. The stress–strain relation for an element is considered linear elastic until the given damage threshold is attained, and then is modified by softening. In RFPA, damage of elements in tension or shear is initiated when its state of stress satisfies the maximum tensile stress criterion or the Mohr–Coulomb criterion, respectively, in order to capture the principal modes of damage and fracture of rock, and the tensile stress criterion is considered preferentially.

The elastic modulus of an element degrades monotonically as damage evolves, and the elastic modulus of damaged material is expressed as follows

$$E = (1 - \omega)E_0, \tag{5}$$

where ω represents the damage variable, and E and E_0 are the elastic module of the damaged and the undamaged material, respectively. The element as well as its damage is assumed isotropic, so the E, E_0 and ω are all scalar. To avoid the problem caused by zero elastic modulus, when $\omega = 1.0$ in Eq. (5), the elastic modulus of a damaged element is specified to a small number, such as $1.0 \times$
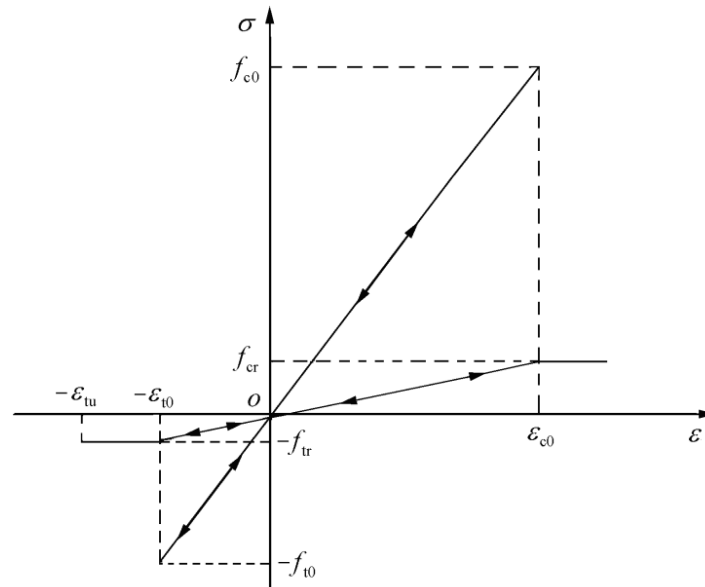

Fig. 5 Elastic damage constitutive law of element subjected to uniaxial stress. f_{t0} and f_{tr} are uniaxial tensile strength and residual uniaxial tensile strength of the element, respectively, and f_{c0} and f_{cr} are uniaxial compressive strength and residual corresponding strength of element, respectively

10^{-5} MPa in our numerical simulation. The sign convention used throughout this paper is that compressive stress and strain are positive. When the mesoscopic element is in a uniaxial stress state (both uniaxial compression and uniaxial tension), the constitutive relation of elements is illustrated as in Fig. 5. Initially, the stress- strain curve is linearly elastic and no damage exists, i.e., $\omega = 0$. When the tensile stress in an element reaches its uniaxial tensile strength, f_{t0}, damage occurs

$$|\sigma_3| \le f_{t0}. \tag{6}$$

The damage variable ω of the element under uniaxial tension, as shown in the third quartile of Fig. 5, can be expressed as

$$\omega = \begin{cases} 0, & \varepsilon > \varepsilon_{t0}, \\ 1 - \dfrac{\lambda \varepsilon_{t0}}{\varepsilon}, & \varepsilon_{tu} < \varepsilon \le \varepsilon_{t0}, \\ 1, & \varepsilon \le \varepsilon_{tu} \end{cases} \tag{7}$$

where λ is the residual tensile strength coefficient, which is given as $f_{tr} = \lambda f_{t0}$. The parameter ε_{t0} is the strain at the elastic limit, and can be called the threshold strain. ε_{tu} is the ultimate tensile strain of the element, describing the state at which the element would be completely damaged. The ultimate tensile strain is defined as $\varepsilon_{tu} = \eta \varepsilon_{t0}$, where η is called the ultimate strain coefficient. In the post-proposing pictures output from RFPA, the elements whose tensile strain attains ε_{tu}, are displayed as black and considered as cracks.

In order to study the damage of an element when it is under compressive and shear stress, the Mohr-Coulomb criterion, expressed as follows, is chosen to define the second damage threshold

$$\sigma_1 - \frac{1 + \sin\varphi}{1 - \sin\varphi}\sigma_3 \ge f_{c0}, \tag{8}$$

where σ_1 and σ_3 are the major and minor principal stress, respectively, f_{c0} is the uniaxial compressive strength and φ is the internal friction angle of the mesoscopic element. When the state of stress in an element satisfies the Mohr-Coulomb criterion, expressed by Eq. (8), the shear damage will occur. The expression for damage variable ω can be described as

$$\omega = \begin{cases} 0 & \varepsilon < \varepsilon_{c0} \\ 1 - \dfrac{\lambda \varepsilon_{c0}}{\varepsilon} & \varepsilon \ge \varepsilon_{c0} \end{cases}, \tag{9}$$

where λ is also the residual strength coefficient, and $f_{cr}/f_{c0} = f_{tr}/f_{t0} = \lambda$ is assumed to apply true when the element is under either uniaxial compression or tension.

During the numerical simulation of RFPA, the specified load (or displacement) is applied to the specimen step by step. In the elastic finite element analysis, the displacements are computed at each node and the stress components in each element. If an element is damaged at a certain load step, the stress distribution is updated and the damage threshold is rechecked for all other elements. If there are other elements that damage, the stress redistribution is continued. This iteration continues until no more new damage in other elements occurs, before the next loading step is applied. By this means, the process of progressive failure of rock subjected to gradually increasing

static loading can be simulated in term of damage. Only for the elements whose tensile strain attains ε_{tu}, they will be displayed as cracks with black color. A user-friendly pre- and post-processors are integrated in RFPA^{2D} to prepare the input data and display the results of the computation. Based on the previous version of RFPA^{2D}, some functions for DIP and assistant modeling are added.

Some validation studies on typical laboratory tests of rock and concrete have been conducted to test the formulation of fracture evolution and rock failure (Tang 1997, Zhu and Tang 2002, Tang and Hudson 2002). It has been found that, under a variety of static loading conditions, the model can effectively simulate the key features of deformation and failure in quasi-brittle materials such as rock and concrete, including non-linearity of stress-strain response, localization of deformation, strain softening, and the crack propagation process.

In RFPA^{2D}, because a damaged element must release the elastic energy stored during deformation, damage of each element is assumed to represent a source of an AE event. Therefore, by recording the number of damaged elements and the associated amounts of energy release, RFPA^{2D} is capable of simulating AE activity including the AE event rate, magnitudes of microseismic events and their location (Tang 1997, Zhu and Tang 2004). In the numerical simulations of rock failure, the AE distributions of some specimens are also used to indicate the locations of damage initiation and the paths of propagation during the failure process.

3. Numerical examples

In the section, three numerical examples are presented to demonstrate the capability of the numerical method proposed in the previous sections in simulating rock failure process and studying the effect of heterogeneity on mechanical behaviors and failure mechanism. The first two examples are the simulation of compressive tests without and with confining pressure, respectively, and the third one is to simulate Brazilian test of rock.

3.1 Numerical specimen of granite

Fig. 6 presents the numerical specimen of granite built based on the image microstructure as shown in Fig. 3, which is composed of 150×300 elements. In Fig. 6, gray level indicates the magnitude of elastic modulus of the elements. The higher the brightness of one element is, the bigger the magnitude of elastic modulus is. The mechanical properties of the three mineral are listed in Table 1 and therefore, the white represents quartz, the dark gray is mica and the intermediate color between the them represents feldspar. In the model, each mineral is considered as a homogeneous material and the heterogeneity contributed by the properties of the three minerals is taken into account. In this numerical specimen, the proportions of quartz, feldspar and mica are 45.9%, 44.4% and 9.7%, respectively, which are calculated by counting their occupied area within the specimen based on the DIP technique.

3.2 Boundary conditions

The first two numerical examples (i.e., uniaxial compressive test and axial compressive tests under different confining pressures) are simulated as plane stress problem. Boundary conditions for the first numerical example are: the bottom boundary is fixed in the vertical direction, while an axial displacement is applied on the upper boundary at a constant rate of 0.001 mm/step, and the
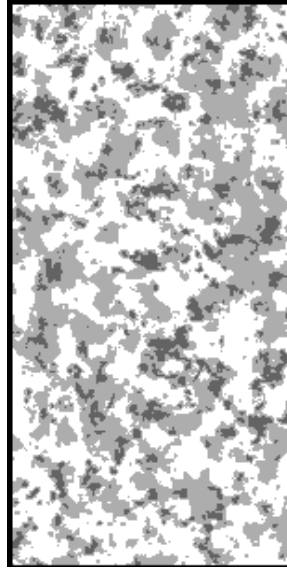
Fig. 6 Numerical specimens of granite built in the RFPA^{2D} code (☐ Quartz; ▨ Feldspar; ■ Mica)

Table 1 Mechanical properties of the three kinds of minerals

Mineral type	Elastic modulus /GPa	Compressive strength /MPa	Tensile strength /MPa	Friction angle /°	Poisson's ratio
Quartz	96	373	24	60	0.08
Feldspar	67	172	14	40	0.27
Mica	40	90	9	30	0.25

two lateral boundaries are free in the horizontal direction. In this regard, the external displacement is applied gradually in the axial direction until the numerical specimen loses its load-bearing capability completely. In the second one, besides the same boundary conditions in vertical direction as those in the 1st one, the confining pressures are applied on the lateral boundaries. For comparison, confining pressures are different in each simulation, which are equal to 2.0 MPa, 4.0 MPa, 6.0 MPa, 8.0 MPa, 10.0 MPa and 15.0 MPa, respectively. The confining pressure is applied step by step with an increment of 0.5 MPa at both lateral sides of the numerical specimen, until the specified values are applied.

3.3 *Numerical simulation under the uniaxial compression*

3.3.1 *Influence of microstructure on stress distribution*

Fig. 7 presents major principal stress (Fig. 7(a)), minor principal stress (Fig. 7(b)) and maximum shear stress (Fig. 7(c)), respectively, when the applied external displacement is 0.001 mm. The gray scale level indicates the magnitude of stress. It can be found that although three minerals are represented as different homogeneous materials, there also exists stress concentration at the boundaries between them. The brighter region of the major principal stress in the specimen (as shown in Fig. 7(a)) are generally vertically distributed, parallel to the loading direction, while
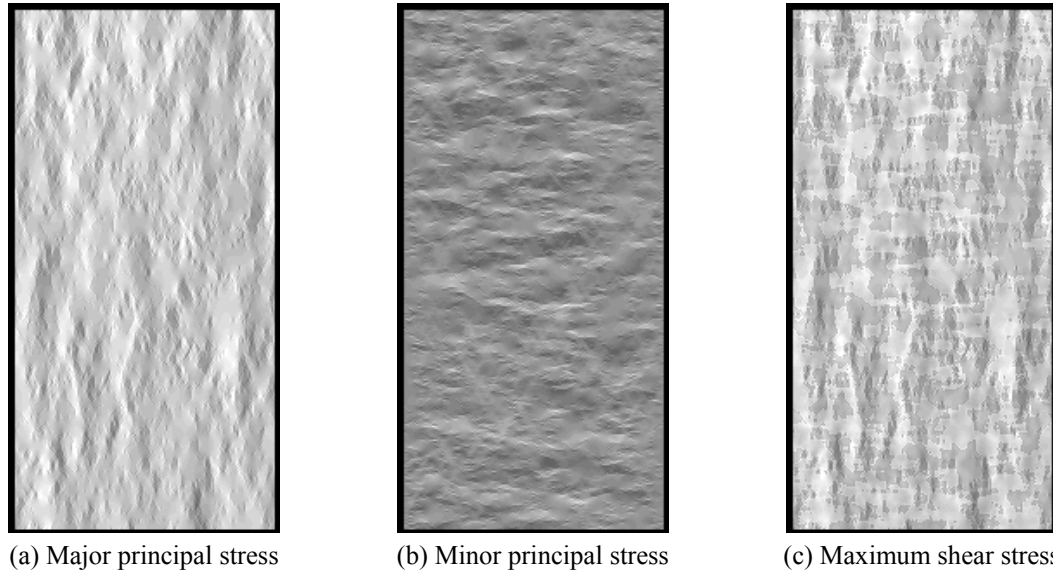
(a) Major principal stress   (b) Minor principal stress   (c) Maximum shear stress

Fig. 7 Stress distribution in the specimen when the applied displacement is 0.001mm in vertical direction
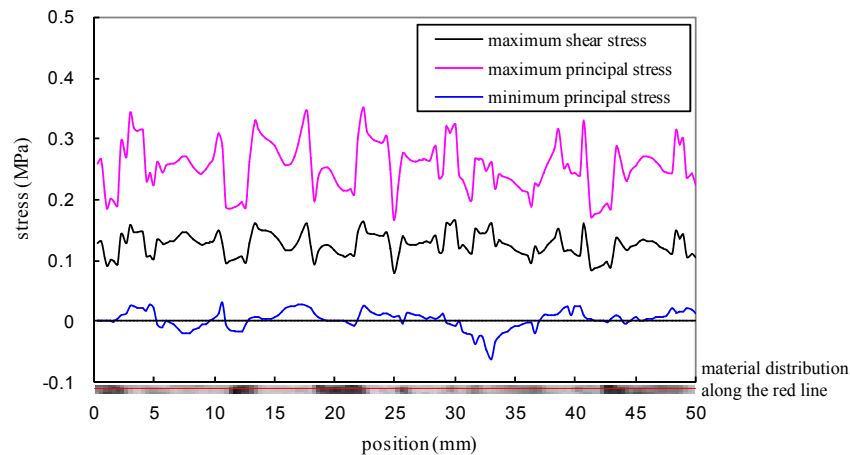

Fig. 8 Stress variable curve along the red line at a 12 mm distance from the top end when applied
displacement is 0.001 mm, and the grain distribution corresponding with *x* coordinate is given

the brighter of minor principal stress (Fig. 7(b)) distributed in a X-shaped region. It is observed that the heterogeneous microstructure of granite has a great influence on stress distribution.

Fig. 8 shows the stress distribution along the horizontal red line (as plotted in Fig. 1(a)) at 12 mm below the upper boundary. For the convenience of illustration, the distribution of mineral grains is also plotted on the abscissa axis. It is observed that the curves usually fluctuate at the boundaries between the two different mineral grains. Within each kind of mineral material, stress distribution is not uniform. It is noted that the minor principal stress is tensile at the *x* coordinates ranging from 5.33 mm to 9.67 mm, 11.0 mm to 12.67 mm and 29.33 mm to 37 mm, respectively, denoting the tensile stress appearing in the numerical specimen although the numerical specimen

is subjected to uniaxial compressive loading. Fig. 9 visualizes the stress distribution within the granite specimen, in which the pink and yellow colors stand for tensile and compressive stress zone, respectively. There exists a large tensile stress zone in the specimen under uniaxial compressive loading condition which may dominate damage evolution and failure mode of rock. Therefore, rock heterogeneity plays an important role in stress distribution.

3.3.2 Numerical results

Fig. 10 shows the stress-strain curve and the associated AE events for the numerical specimen under uniaxial compression. The elastic modulus and uniaxial compressive strength of this numerical specimen could be calculated as 73.35 GPa and 67.37 MPa from this stress-strain curve,
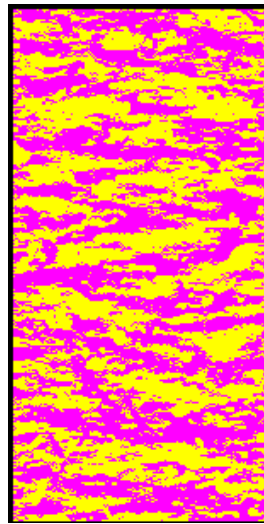

Fig. 9 Distribution of tensile stress zone in the granite specimen under uniaxial compression
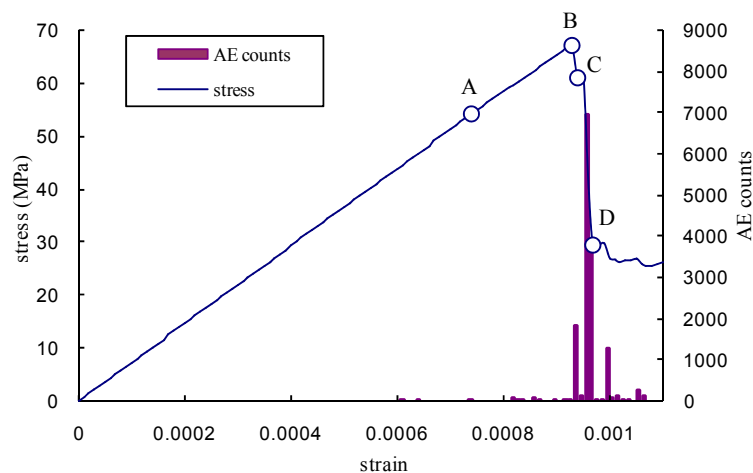(■ tensile stress; □ compressive stress)

Fig. 10 Stress-strain curve and the associated AE events of the granite sample under uniaxial compression

respectively. It can be seen clearly that there is a good relation between the simulated stress–strain curve and the AE event rate: every large stress drop in the stress-strain curve corresponds to a high event rate. Although some AE events occur at approximately 66% peak load, they release little elastic strain energy. Therefore, the stress-strain curve stays nearly linear up to the peak load. But at post-peak region, high AE event rates appear, corresponding to three large stress drops in the stress-strain curve. After this, the load-bearing capacity drops rapidly, followed by low residual strength. This characteristics of the stress-strain curve and associated AE events in rock specimen under uniaxial compression have been reported in previous experimental observations or numerical simulations (Blair and Cook 1998, Potyondy and Cundall 2004, Potyondy *et al*. 1996, Fang and Harrison 2002, Tang 1997, Zhu and Tang 2002, 2004, Tang *et al*. 2000). Thus it confirms that the proposed DIP-based numerical method is capable in simulating the stress-strain curve and associated AE events during the failure of heterogeneous rock under uniaxial compression.

Fig. 11 shows the elastic modulus (Fig. 11(a)), maximum shear stress (Fig. 11(b)) and AE events (Fig. 11(c)) during the progressive failure process of the numerical specimen at the stress levels denoted with 'A'-'D' as labeled in Fig. 10. It is observed that the isolated cracks firstly occur at the boundaries between the mica and feldspar grains (i.e., inter-granular cracks) at the loading level A (the applied external displacement is 0.075 mm, Fig. 11(a)-A and Fig. 11(b)-A). When the loading level reaches peak stress at point B, some clustered cracks come into being, which locate at the right top and left bottom of the numerical specimen (Fig. 11(a)-B and Fig. 11(b)-B). Inter-granular and trans-granular cracks can be both found at this stage. The cracks propagate not only through the weak minerals or along grain boundaries, but also penetrate through the high-strength stiff quartz or feldspar (i.e., trans-granular cracks) when the crack propagation is blocked by the strong mineral. At the post-peak stage, some isolated fractures continue to come into being, and propagate in a direction nearly parallel to the loading direction and the trans-granular crack propagations become common phenomena (Fig. 11(a)-C and Fig. 11(b)-C). Some splitting cracks propagate and coalesce with the top boundary of the specimen, leading to the formation of a local macroscopic failure plane near the left boundary of the specimen, similar to spalling of rock wall (Fig. 11(a)-D and Fig. 11(b)-D). Finally, the specimen lost its bearing capability until another shear failure band near the left-top boundary of the specimen, which consists of many splitting cracks, is also formed to coalesce with the above mentioned fracture plane (Fig. 11(a)-D and Fig. 11(b)-D).

Fig. 11(c) shows the spatial distribution of the AE events during the uniaxial loading. Each circle represents one AE event and the diameter of the circle represents the relative magnitude of the released AE energy. Each AE event means that the stress state of one element violates its strength threshold and damage occurs, thus releasing its strain energy as the acoustic emission. In this respect, red and white are for tensile and shear damage at current step, respectively, and the black is for being damaged in all preceding steps. As we predicted above, the tensile stress firstly reaches the tensile strength of some elements and tensile damage occurs, which is shown in Fig. 11 (c)-A. It is observed that most of the elements are damaged in tension, and only few elements damaged in shear mode randomly exist during the failure process. Finally, a macroscopic shear fracture plane is formed, as shown in Fig. 11(c)-D, however, in which most of the elements are damaged in tension. That is to say, macroscopic shear fracture planes observed in brittle rock (e.g., granite) under uniaxial compression result from the interaction and coalescence of tensile damage due to the effect of rock heterogeneity at the mesoscopic level. This numerical simulation result is very similar to those observed in AE experiments (Lockner *et al*. 1992, Glover *et al*. 2000) and

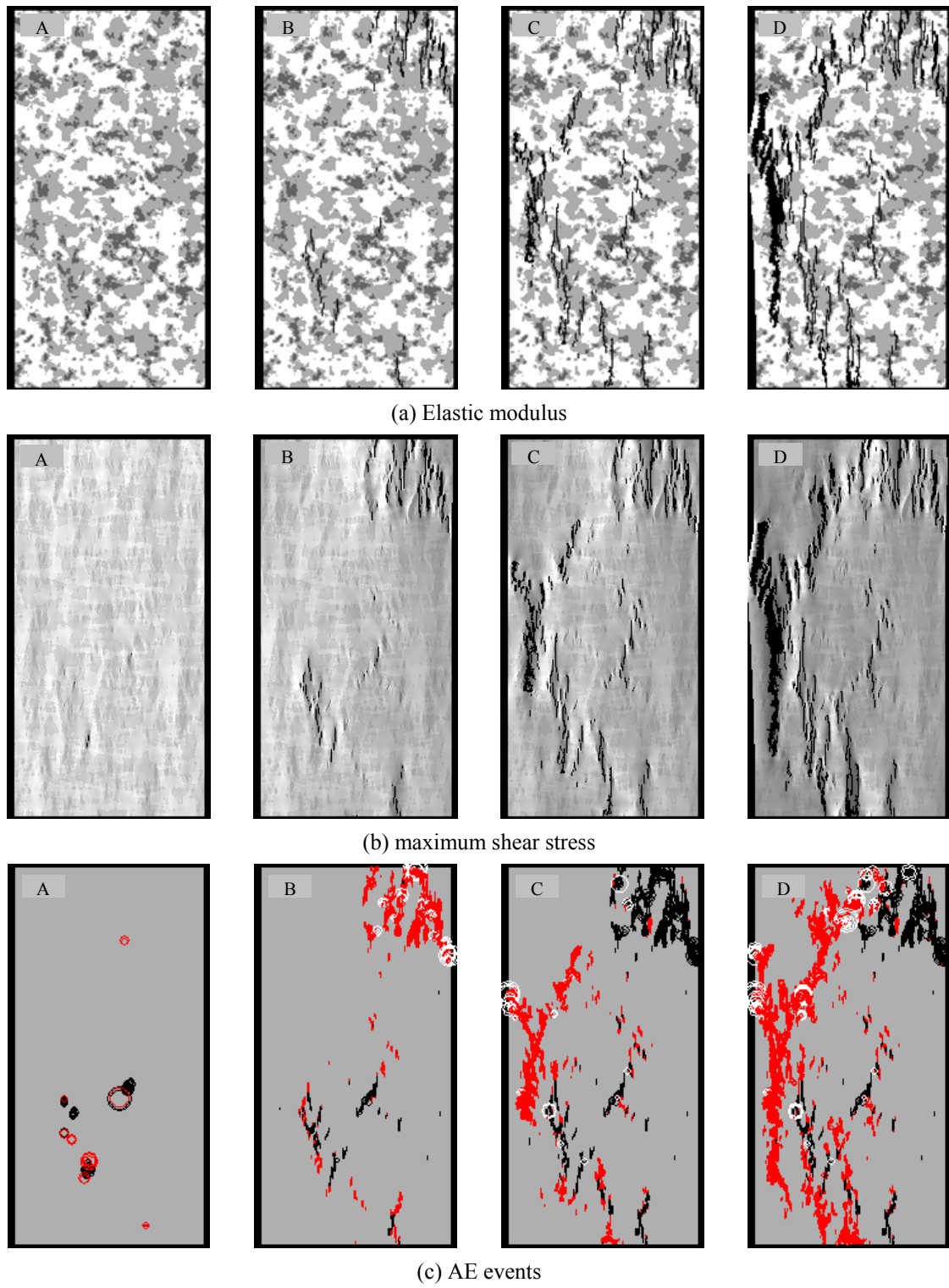(a) Elastic modulus

(b) maximum shear stress

(c) AE events

Fig. 11 Progressive failure process of the granite specimen under uniaxial compression

obtained with image-analysis techniques (Moore and Lockner 1995). Also it should be noted that most of elements are damaged in tensile mode, thus confirming the importance of tensile damage during the uniaxial compression test of rock. In particular, this associated damage mechanism can only be captured when the rock heterogeneity is taken into account with DIP-based technique.

3.4 Numerical simulation on compression test under confining pressure

In this section, compressive tests under lateral confining stress are numerically simulated to illustrate the effect of heterogeneity and confining pressure on the rock failure mechanism. For convenient illustration, the coefficient of lateral pressure k is defined as the ratio of confining pressure to axial stress.

(a) $k = 0.01$ (b) $k = 0.02$ (c) $k = 0.05$ (d) $k = 0.1$ (e) $k = 0.2$
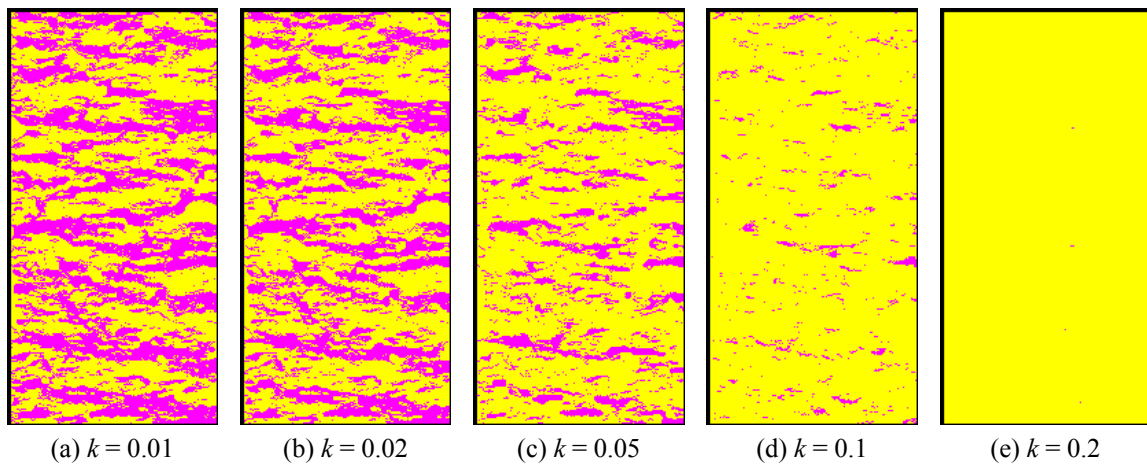
Fig. 12 Distribution of tensile stress zone in the granite specimen under different lateral pressure coefficients: ▢ tensile stress, ▢ compressive stress
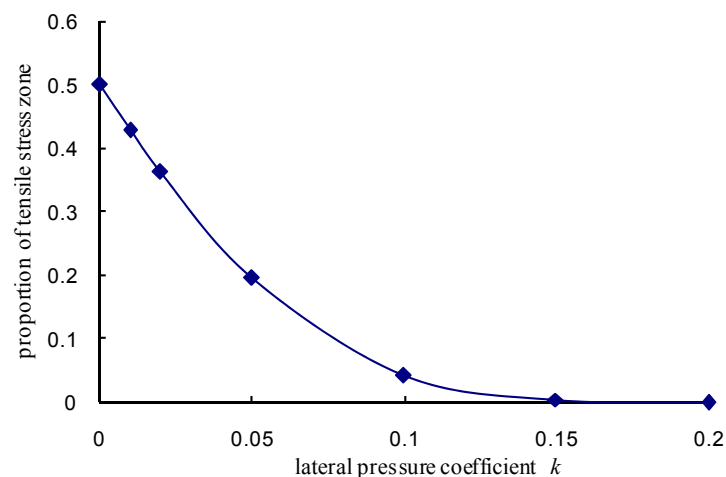

Fig. 13 Proportion of area of tensile stress zone in the specimen under different lateral pressure coefficient k

3.4.1 Effect of confining pressure on tensile stress distribution

Fig. 12 shows the distribution of tensile stress zone in the granite specimen under different lateral pressure coefficients, in which the pink and yellow colors indicate tensile and compressive stress zone, respectively. It is observed that the tensile stress zone becomes smaller; the compressive stress zone, however, becomes larger under increasing confining stress.

As shown in Fig. 13, under the uniaxial compressive loading, the area of tensile stress zone is more than 50%. By contrast, it is gradually reduced with the increasing lateral pressure coefficient, and it occupies only 0.01% under the lateral pressure coefficient of 0.2. It indicates that confining stress plays a dominant role in restraining the tensile stress in the rock specimen.

3.4.2 Failure mechanism

Fig. 14 shows the numbers of damaged elements under different lateral pressure coefficients, which are normalized with its total number of damaged elements. Under the low or intermediate confining pressure, there exists shear damage in addition to the tensile damage. As confining pressure increases, the tensile stress zone induced by rock heterogeneity is restrained, and therefore, the number of elements damaged in tension declines gradually and that of shear damage increases (Fig. 14). As shown in Fig. 14, when the lateral pressure coefficient is smaller than 0.06, tensile damage is dominant during rock failure process; however, when it increases beyond 0.06, shear damage becomes dominant gradually. In this regard, rock failure mechanism actually changes from tensile damage to shear damage under the higher confining pressure.

Fig. 15 shows the failure modes of granite under different confining pressure. Under unconfined compression, rock specimen shows typical brittle tensile failure, and fracture plane is approximately parallel to the direction of the major principal stress (Fig. 15(a)). Under the higher confining pressure, the fracture of rock specimen transits from shear-tensile damage (i.e., tensile damage is dominant over shear one, as shown in Fig. 15(b)) to tensile-shear damage (i.e., shear damage is dominant over tensile damage, as shown in Fig. 15(c)), and gradually tends to typical shear failure pattern (Figs. 15(d) and (e)) or failure pattern with multiple shear surfaces (Figs. 15(f) and (g)). Under the higher lateral pressure coefficient, the X-shaped failure planes are formed in
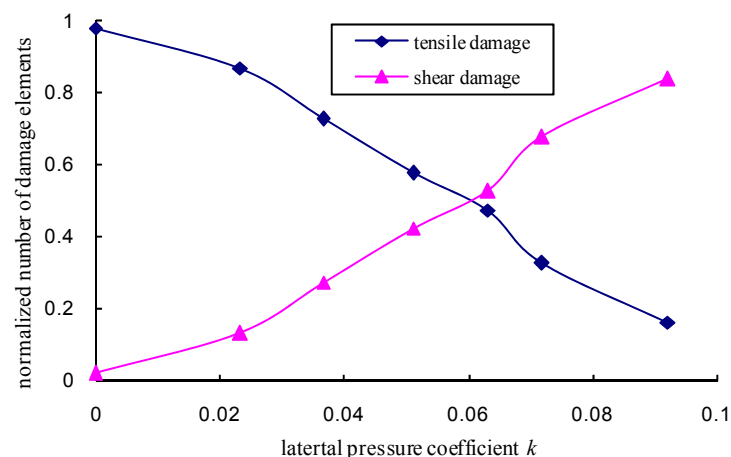

Fig. 14 Normalized number of tensile failure and shear failure elements with different lateral pressure coefficient *k*

(a) $\sigma_3 = 0$ MPa   (b) $\sigma_3 = 2$ MPa   (c) $\sigma_3 = 4$ MPa   (d) $\sigma_3 = 6$ MPa

(e) $\sigma_3 = 8$ MPa   (f) $\sigma_3 = 10$ MPa   (g) $\sigma_3 = 15$ MPa   (h) orientation of failure plane
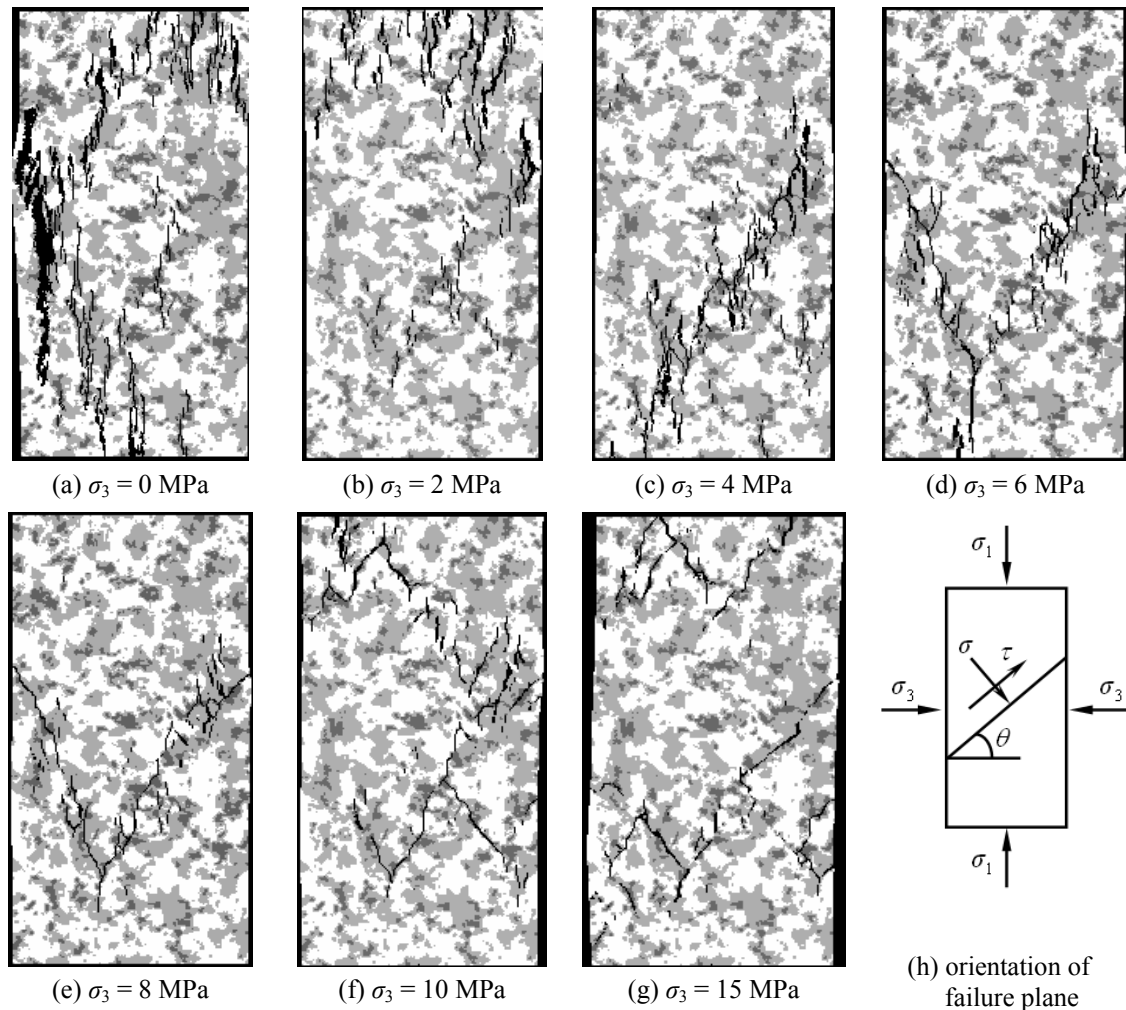
Fig. 15 Failure patterns of granite under different confining pressures (numerical results)

the numerical specimen. Moreover, it is found that the orientation angle of failure plane also decreases with the confining pressure. This complex rock failure mechanism results from the combined contribution of rock heterogeneity and confining pressures.

3.5 Numerical simulation on Brazilian test

Brazilian test is generally accepted to measure the quasi-static tensile strength of rock-like materials (ISRM 1978). In this section, Brazilian test is simulated and the effect of heterogeneity on the stress distribution along vertical diametrical axial and failure process is investigated.

3.5.1 Brazilian test model

Fig. 16(a) is a color granite digital image retrieved from the cross-section of a cylinder specimen with a diameter of 50 mm. The digital image is composed of 150×150 pixels. Because

(a) digital image from the cross-section of a granite specimen

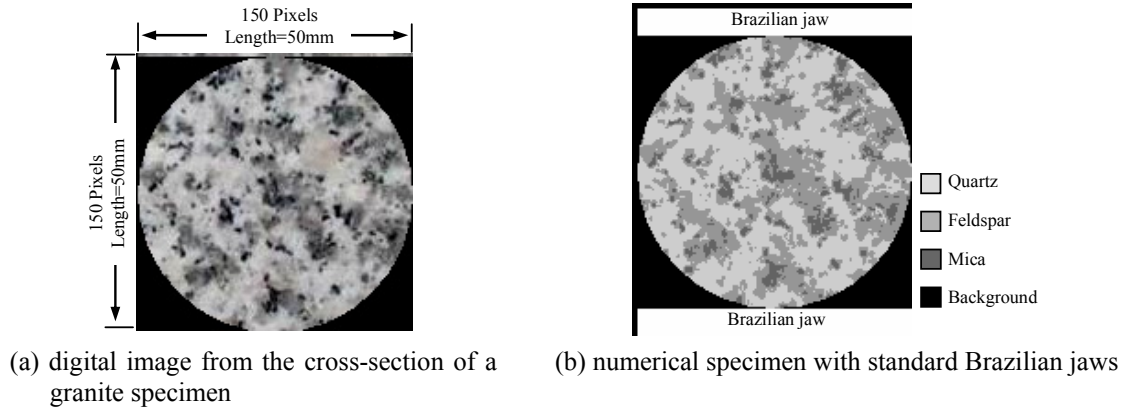(b) numerical specimen with standard Brazilian jaws

Fig. 16 Numerical model for Brazilian test

this cylinder specimen is the same type granite as the one shown in Fig. 1(a)), the segment thresholds of *I* values are also selected as 100 and 170. Based on the DIP-based technique, the numerical specimen of Brazilian test is built and shown in Fig. 16(b). A pair of jaws for loading is attached on the rock specimen. The bottom of the lower jaw is fixed in vertical direction and a vertical external displacement at a rate of 0.0001 mm/step is applied on the top of the upper jaw step by step, until the rock disc loses its load-bearing capability completely.

3.5.2 Numerical results

If rock material is assumed homogeneous, isotropic and linear elastic, the stress components σ_x and σ_y along the loading diameter under the Brazilian test, is obtained as (Jaeger and Cook 1976)

$$\sigma_x = -\frac{2P}{\pi dt} \tag{10}$$

$$\sigma_y = \frac{2P}{\pi t}\left(\frac{1}{r_1} + \frac{1}{r_2}\right) - \frac{2P}{\pi dt} \tag{11}$$

where *P* is the applied load; *d* and *t* are the diameter and thickness of the rock disc, respectively; r_1 and r_2 are the distance of one point located on the vertical diameter from the upper and lower end of the disc, respectively, and their sum is equal to *d*.

It is generally accepted that the tensile strength of rock is much lower than its compressive strength. Therefore, if the disc is to fail due to the tensile stress σ_x, the tensile strength of the disc can be calculated as

$$\sigma_t = \sigma_x = -\frac{2P_{max}}{\pi dt} \tag{12}$$

where P_{max} is the load required for failure.

During the numerical simulation, when the external placement of 0.0001 mm / step is applied on the top surface of upper jaw, the resultant load is calculated as 1.421 N. Therefore, according to Eqs. (10) and (11), stress distribution along the vertical diameter can be theoretically evaluated. Analytical solutions and DIP-based numerical results of the stress are plotted together, as shown in

Figs. 17(a) and (b). It is found that if the end effect during loading is ignored, numerical results from the DIP-based approach compare favorably with the analytical results. However, due to the rock heterogeneity induced by mineral grains distribution (indicated by the red solid line in Fig. 17), the stresses are varying on the vertical loading diameter and fluctuating around the analytical results, especially at the grain boundaries. Comparing the numerical results in Figs. 17(a) and (b), it can be observed that the distribution curve of σ_x fluctuates more obviously than σ_y, which implies that mineral grains distribution has a greater influence on tensile stress than compressive stress. Furthermore, the position of maximum tensile stress has deviated from the midpoint of the vertical diameter, and therefore when maximum tensile stress attains tensile strength, damage may not initiate at the center of Brazilian disc.

From the numerical simulation of Brazilian test, the maximum load is obtained as 374.827 N, and the parameter t in Eq. (12) is unit thickness in two-dimensional model, based on which the tensile strength is calculated as 2.386 MPa. This strength obtained by the proposed DIP-based method is far smaller than the tensile strength of each mineral constituent. The reason is that the stress concentration induced by mineral grains distribution results in the tensile failure concentration under a lower loading level.

The numerical results of the failure process of the granite disc are shown in Fig. 18, in which

(a) σ_x distribution
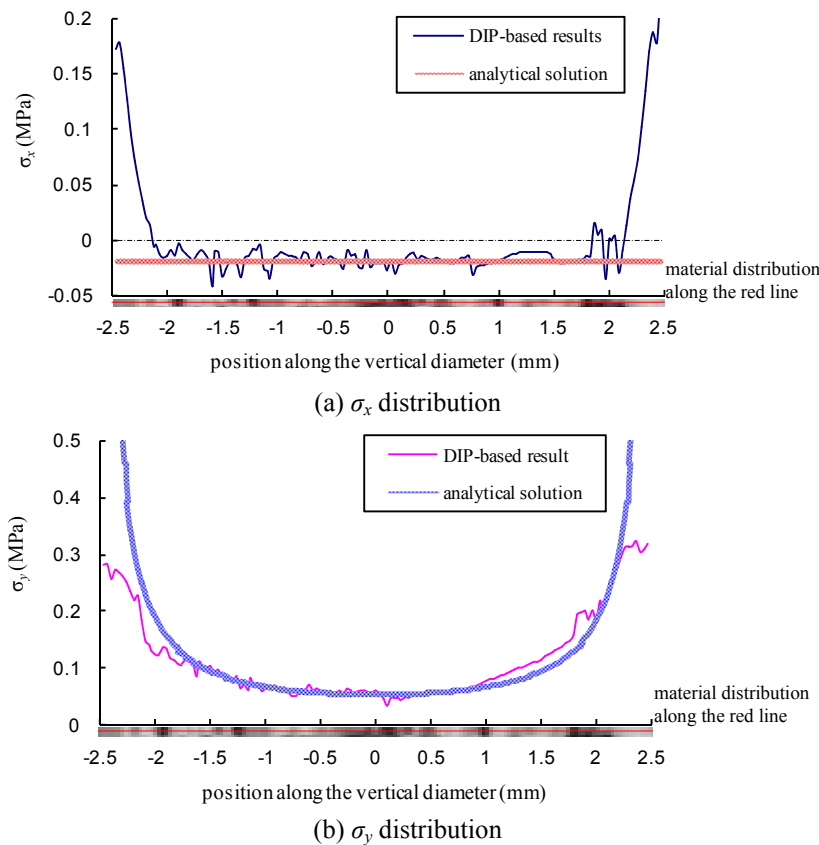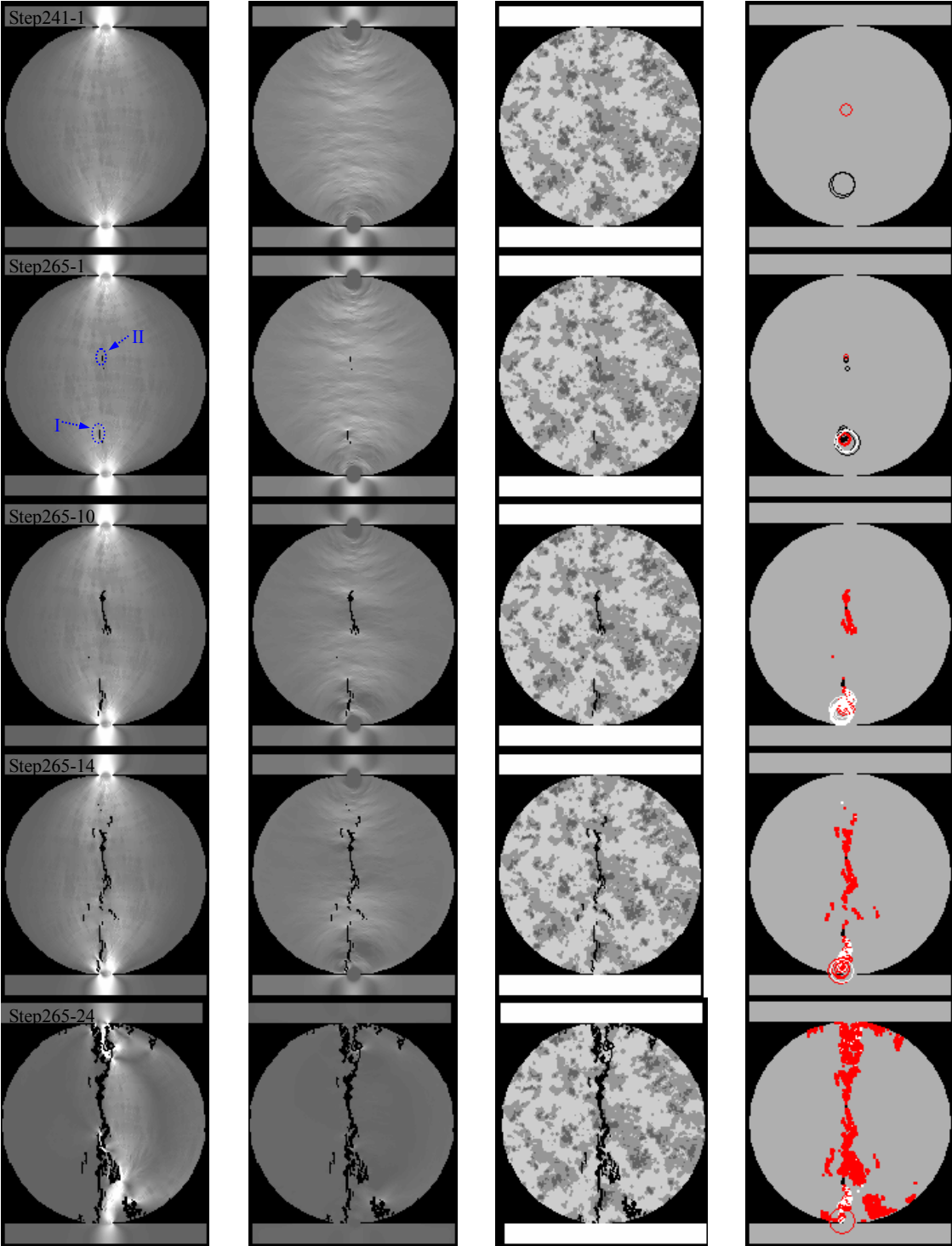

(b) σ_y distribution

Fig. 17 Comparison of Stress distribution obtained by the proposed model with the analytical solution for homogeneous specimen along the vertical diameter

(a) Maximum shear stress   (b) Minor principal stress   (c) Elastic modulus   (d) AE events

Fig. 18 Splitting process of granite disc simulated by the DIP-based method

the maximum shear stress (Fig. 18(a)), minor principal stress (Fig. 18(b)), elastic modulus (Fig. 18(c)) and AE events (Fig. 18(d)), are shown. In this figure, the notation Step 241-1 indicates that this is at the 1th iterative step in the 241st loading step. With the increase of external displacement, the initial shear damage occurs at Step 234-1 at the boundary between mica and feldspar, which is located near the bottom end of rock disc, as indicated by the circles with black color (at Step 241-1 in Fig. 18(d)). It is also on the boundary between mica and feldspar that tensile damage occurs, located near the center of the disc (the red circle at Step 241-1 in Fig. 18(d)).

At Step 265 several iterative steps are included. Firstly the two cracks formed by the damaged elements at two locations propagate in vertical direction (Step265-1 in Figs. 18(a), (b) and (c)), which are denoted by I and II at step 265-1 in Fig. 18(a). But because there is strong mineral grain (quartz) on the upper tip of crack I (at Step 265-10 in Fig. 18(c)), the crack only propagates downwards, whilst crack II propagates both upwards and downwards. Two cracks propagate along the boundaries between mineral grains and also penetrate relative weak mineral grains (at Step 265-14 and Step 265-24 in Fig. 18(c)). Finally, the main fracture zone is formed (at Step 265-24 in Fig. 18), which results in losing the load-bearing capability of rock disc.

From the observation at macroscopic level, the numerical disc is split into two main parts, as shown at Step 265-24 in Fig. 18, thus confirming that this is a valid Brazilian test. However, during the formation and growth of crack I, shear damage also emerges at the cracking path, as denoted by the while circles at Step 265-1 and Step 265-10 in Fig. 18(d), respectively. In particular near the lower and upper end of the disc, where compressive stress is highly concentrated, many shear damaged elements (at Step 265-24 in Fig. 18(d)) are found. Moreover, some scattered shear damaged elements also exist in the splitting zone. In a word, although the whole failure under the Brazilian test is dominated by the tensile damage near the loading diameter of rock disc, there also exists some shear damage during the failure process of Brazilian disc. In this respect, many scholars had suggested other failure mechanism except tensile failure exist in Brazilian test (Fairhurst 1964, Mellor and Hawkes 1971), the numerical simulation of this study highlight this opinion when the rock heterogeneity is incorporated in the numerical model.

In the numerical simulation of RFPA with DIP-based technique, the Mohr-Coulomb criterion and the maximum tensile stress criterion, as expressed in Eqs. (6) and (8), are adopted to judge the stress conditions of each element. During the Brazilian test, the elements in rock disc are under the biaxial stress condition, where the major principal stress (σ_1) is positive (compressive) and the minor principal stress (σ_3) is negative (tensile). In particular, for some elements with high tensile strength (e.g., quartz mineral grains), the minor principal stress (σ_3) is not high enough to attain the maximum tensile stress criterion, the shear damage may occur when the stress state of element meets the Mohr-Coulomb criterion. For example, white circles in Fig. 18(d) illustrates that shear failure mechanism also exists in Brazilian test. Moreover, Lilliu *et al*. (1999), Vasil'ev and Nikiforovskii (2001) also thought that the Mohr-Column like fracture law must be used in their models in order to effectively simulate the failure in Brazilian test.

3.6 Discussion

It is obvious that, detailed description of heterogeneous microstructure is really essential when we try to model the mechanical behavior and fracture process of real heterogeneous material. In this study, DIP technique is employed to characterize rock heterogeneity by using the digital image of a rock sample, which can take the real microstructure of rock into account to a great extent. Based on that, the numerical specimen of this rock is established in the RFPA[2D] code, in

order to reproduce the mechanical behavior and failure process of rock under a variety of loading conditions.

However, due to the resolution of the image, only the geometry of mineral grains (e.g., quartz, feldspar and mica) and their properties have been taken into account in the model in order to describe the rock heterogeneity. It has been found that this heterogeneity plays an important role in stress distributions in crystalline rocks such as granite. In particular, when rock heterogeneity is taken into account, tensile damage is easily induced within the rock even it is under compressive loading condition, which may further influences the strength and damage evolution. In this respect, grain boundaries act as the predominant source of stress concentration and preferable location of tensile damage initiation. The first detectable fracturing starts at the grain boundaries and inter-granular cracks also occur at the locations of weak mineral constituents such as feldspar and mica grains. Direct observations of micro-fractures using optical microscopes, scanning electron microscopes (SEM) or other petrographic techniques have led to similar conclusions as to which grain boundaries constitute the weakest planes and are therefore most prone to fracture propagation (Eberhardt *et al.* 1999, Li *et al.* 2002). In fact, besides these heterogeneous constituents, there also exist voids, microcracks and other defects within rock, which may also result in rock heterogeneity. The proposed model is based on the digital image of rock and all information of microstructure it reflects can be taken into account in the model. Therefore, the detailed characterization of the rock heterogeneity and microstructure depends on the resolution of digital image of rock. It is known that images captured by scanning electron microscopes (SEM) can provide more specific detailed information, and the computerized tomography (CT) is possible to provide the 3D image of rock sample. As a result, if the digital images retrieved with CT are used to build the numerical specimen, it can reflect the more detailed 3D microstructure of rock, which will be helpful to deeply understand the mechanical behavior and fracture process that are associated with the rock heterogeneity.

4. Conclusions

In this paper, DIP technique is proposed to characterize the heterogeneity of actual rock sample, based on which the rock failure process is numerically simulated with RFPA by taking the actual material heterogeneity into account. The aim is to improve our understanding of the role of rock heterogeneity in the damage and failure process of rock. Taking granite sample as an example, three simulation examples are presented, based on which, the following conclusions are drawn:

(1) Rock heterogeneity plays a significant role in stress distribution, which results in tensile stress even under uniaxial compression. Under uniaxial compression, the failure mechanism of granite specimen is mainly tensile failure at the meso-scale level and the macroscopic shear band results from the cluster of tensile damage at the meso-level;

(2) The confining stress plays a dominant role in the stress distribution in the rock specimen, which may restrain the tensile stress induced by rock heterogeneity. Under low or medium confining pressure, there exists not only tensile failure but also shear failure at the meso-scale level. With the increase in confining pressure, the failure mode changes from tensile failure to shear failure, and then shear failure becomes dominant;

(3) The simulation of Brazilian test shows that, the shear failure mechanism also exists in Brazilian test of granite near the lower and upper end of a disc where the compressive stress is highly concentrated, and therefore the Mohr-Column criterion must be used in

order to effectively simulate the shear failure in Brazilian test.

The DIP-based numerical method proposed in this paper is of strong capability to study rock failure behavior by taking the actual heterogeneity of rock into account, which provides an innovative tool for predicting the mechanical behaviors of rock and rock-like materials affected by its microstructures. Although the accuracy of microstructure characterization of rock depends on the resolution of the digital images, it is also limited by the computational capacity of the computers. However, this could be improved when the high-resolution digital images could be retrieved with advanced photographic facilities and RFPA code could be run under the high-performance computing (HPC) environment.

References

Blair, S.C. and Cook, N.G.W. (1998), "Analysis of compressive fracture in rock statistical techniques: Part I: A non-linear rule-based model", *Int. J. Rock Mech. Mining Sci.*, **35**(7), 837-848.

Chen, S., Yue, Z.Q. and Tham, L.G. (2004), "Digital image-based numerical modeling method for prediction of inhomogeneous rock failure", *Int. J. Rock Mech. Mining Sci.*, **41**(6), 939-957.

Chinaia, B., Vervuurt, A. and Van Mier, J. G.M. (1997), "Lattice model evaluation of progress failure in disordered particle composites", *Eng. Fract. Mech.*, **57**(2/3), 301-318.

Eberhardt, E., Stimpson, B. and Stead, D. (1999), "Effects of grain size on the initiation and propagation thresholds of stress-induced brittle fractures", *Rock Mech. Rock Eng.*, **32**(2), 81-99.

Fairhurst, C. (1964), "On the validity of the ''Brazilian'' test for brittle materials", *Int. J. Rock Mech. Mining Sci.*, **1**(4), 535-546.

Fairhurst, C. (1997), "Geomaterials and recent development in micro-mechanical numerical models", *News J.*, **4**(2), 11-14.

Fang, Z. and Harrison, J.P. (2002), "Application of a local degradation model to the analysis of brittle fracture of laboratory scale rock specimens under triaxial conditions", *Int. J. Rock Mech. Mining Sci.*, **39**(4), 459-476.

Glover, P.W.J., Gomez, J.B. and Meredith, P.G. (2000), "Fracturing in saturated rocks undergoing triaxial deformation using complex electrical conductivity measurements: Experimental study", *Earth Planet Sci. Lett.*, **183**(1-2), 201-213.

Gonzalez, R.C. and Woods, R.F. (1992), *Digital Image Processing*, Reading, MA, Addison-Wesley.

ISRM (1978), "International society for rock mechanics. Suggested methods for determining tensile strength of rock materials", *Int. J. Rock Mech. Mining Sci.*, Geomech. Abstr., **15**, 99-103.

Jaeger, J.C. and Cook, N.G.W. (1976), *Fundamentals of Rock Mechanics*, Chapman and Hall, London, UK.

Karamnejad, A., Nguyen, V.P. and Sluys, L.J. (2013), "A multi-scale rate dependent crack model for quasi-brittle heterogeneous materials", *Eng. Fract. Mech.*, **104**, 96-113.

Kazerani, T. (2013), "A discontinuum-based model to simulate compressive and tensile failure in

sedimentary rock", *J. Rock Mech. Geotech. Eng.*, **5**(5), 378-388.

Kemeny, J., Mofya, E. and Handy, J. (2003), "The use of digital imaging and laser technologies for field rock fracture characterization", *Proceedings of the 12th Pan-American Conference on Soil Mechanics and Geotechnical Engineering*, Cambridge, MA, USA, June.

Lemy, F. and Hadjigeorgiou, J. (2003), "Discontinuity trace map construction using photographs of rock exposures", *Int. J. Rock Mech. Mining Sci.*, **40**(6), 903-917.

Li, L., Tsui, Y., Lee, P.K.K., Tham, L.G., Li, T.J. and Ge, X.R. (2002), "Progressive cracking of granite plate under uniaxial compression", *Chinese J. Rock Mech. Eng.*, **21**(7), 940-947.

Liang, Z.Z., Xing, H., Wang, S.Y., Williams, D.J. and Tang, C.A. (2012), "A three-dimensional numerical investigation of the fracture of rock specimens containing a pre-existing surface flaw", *Comput. Geotech.*, **45**, 19-33.

Lilliu, G., van Mier, J.G.M. and van Vliet, M.R.A. (1999), "Analysis of crack growth of the Brazilian test: experiments and lattice analysis", *Proceedings of the 8th International Conference on the Mechanical Behavior of Materials*, Victoria, Canada, May.

Lockner, D.A., Byerlee, J.D., Kuksenko, V., Ponomarev, A. and Sidorin, A. (1992), "Observations of quasi-static fault growth from acoustic emissions", *Fault Mechanics and Transport Properties of Rocks*, Academic Press, USA.

Ma, G.W., Wang, X.J. and Ren, F. (2011), "Numerical simulation of compressive failure of heterogeneous rock-like materials using SPH method", *Int. J. Rock Mech. Mining Sci.*, **48**(3), 353-363.

Malan, D.F. and Napier, J.A.L. (1995), "Computer modeling of granular material micro fracturing", *Tectonophysics*, **248**(1/2), 21-37.

Mellor, M. and Hawkes, I. (1971), "Measurement of tensile strength by diametral compression of discs and annuli", *Eng. Geol.*, **5**(3), 173-225.

Molladavoodi, H. and Mortazavi, A. (2011), "A damage-based numerical analysis of brittle rocks failure mechanism", *Finite Elem. Anal. Design*, **47**(9), 991-1003.

Moore, D.E. and Lockner, D.A. (1995), "The role of microcracking in shear-fracture propagation in granite", *J. Struct. Geol.*, **17**(1), 95-114.

Mortazavi, A. and Molladavoodi, H. (2012), "A numerical investigation of brittle rock damage model in deep underground openings", *Eng. Fract. Mech.*, **90**, 101-120.

Pan, P.Z., Yan, F. and Feng, X.T. (2012), "Modeling the cracking process of rocks from continuity to discontinuity using a cellular automaton", *Comput. Geosci.*, **42**, 87-99.

Potyondy, D.O. and Cundall, P.A. (2004), "A bonded-particle model for rock", *Int. J. Rock Mech. Mining Sci.*, **41**(8), 1329-1364.

Potyondy, D.O., Cundall, P.A. and Lee, C. (1996), "Modeling of rock using bonded assemblies of circular particles", *Proceedings of Second North American Rock Mechanics Symposium*, Montreal, QC, Canada, June.

Reid, T.R. and Harrison, J.P. (2000), "A semi-automated methodology for discontinuity trace detection in digital images of rock mass exposures", *Int. J. Rock Mech. Mining Sci.*, **37**(7), 1073-1089.

Schlangen, E. and Garboczi, E.J. (1997), "Fracture simulations of concrete using lattice models: computational aspects", *Eng. Fract. Mech.*, **57**(2/3), 319-332.

Tang, C.A. (1997), "Numerical simulation of progressive rock failure and associated seismicity", *Int. J. Rock Mech. Mining Sci.*, **34**(2), 249-261.

Tang, C.A. and Hudson, J.A. (2002), "Understanding rock failure through numerical simulations and implications for the use of codes in practical rock engineering", *Proceedings of the 5th North American Rock Mechanics Symposium and the 17th Tunnelling Association of Canada Conference*, Toronto, ON, Canada, July.

Tang, C.A., Liu, H., Lee, P.K.K., Tsui, Y. and Tham, L.G. (2000), "Numerical studies of the influence of microstructure on rock failure in uniaxial compression—Part I: Effect of heterogeneity", *Int. J. Rock Mech. Mining Sci.*, **37**(4), 555-569.

Van Mier, J.G.M. (1997), "Fracture processes of concrete: Assessment of material parameters for fracture models", CRC Press Inc., Boca Raton, FL, USA.

Vasil'ev, S.P. and Nikiforovskii, V.S. (2001), "On failure mechanism of specimens in the 'Brazilian test' scheme", *J. Mining Sci.*, **37**(2), 180-183.

Weibull, W. (1951), "A statistical distribution function of wide applicability", *J. Appl. Mech.*, **18**, 293-297.

Yan, F., Feng, X.T., Pan, P.Z. and Li, S.J. (2014), "Discontinuous cellular automaton method for crack growth analysis without remeshing", *Appl. Math. Model.*, **38**(1), 291-307.

Yuan, S.C. and Harrison, J.P. (2006), "A review of the state of the art in modelling progressive mechanical breakdown and associated fluid flow in intact heterogeneous rocks", *Int. J. Rock Mech. Mining Sci.*, **43**(7), 1001-1022.

Yue, Z.Q. and Morin, I. (1996), "Digital image processing for aggregate orientation in asphalt concrete mixtures", *Can J. Civil Eng.*, **23**(2), 479-489.

Yue, Z.Q., Chen, S. and Tham, L.G. (2003), "Finite element modeling of geomaterials using digital image processing", *Comput. Geotech.*, **30**(5), 375-397.

Yue, Z.Q., Chen, S. and Zhen, H. (2004), "Digital image processing based on finite element method for geomaterials(in Chinese)", *Chinese J. Rock Mech. Eng.*, **23**(6), 889-897.

Zhao, G.F., Khalili, N., Fang, J.N. and Zhao, J. (2012), "A coupled distinct lattice spring model for rock failure under dynamic loads", *Comput. Geotech.*, **42**, 1-20.

Zhu, W.C. and Tang, C.A. (2002), "Numerical simulation on shear fracture process of concrete using mesoscopic mechanical model", *Construct. Build. Mater.*, **16**(8), 453-463.

Zhu, W.C. and Tang, C.A. (2004), "Micromechanical model for simulating the fracture process of rock", *Rock Mech. Rock Eng.*, **37**(1), 25-56.

Zhu, W.C., Liu, J., Yang, T.H., Sheng, J.C. and Elsworth, D. (2006), "Effects of local rock heterogeneities on the hydromechanics of fractured rocks using a digital-image-based technique", *Int. J. Rock Mech. Mining Sci.*, **43**(8), 1182-1199.

CC